Calculated and experimental Schmid factors for chip flow deformation of textured CVD α-alumina coatings

Surface & Coatings Technology 412 (2021) 126991

Contents lists available at ScienceDirect

Surface & Coatings Technology

journal homepage: www.elsevier.com/locate/surfcoat

Calculated and experimental Schmid factors for chip flow deformation of textured CVD α-alumina coatings

S. Shoja [a,b,*], O. Alm [c], S. Norgren [b], H.-O. Andrén [a], M. Halvarsson [a]

[a] Department of Physics, Chalmers University of Technology, Gothenburg, Sweden
[b] Sandvik Coromant, Stockholm, Sweden
[c] Seco Tools, Fagersta, Sweden

ARTICLE INFO

Keywords:
α-Al_2O_3
Hard coatings
CVD
Schmid factor
Deformation mechanisms

ABSTRACT

A thorough analysis of Schmid factors (m) for three different (basal and two prismatic) slip systems and three different coating textures, (0001), $(01\bar{1}2)$ and $(11\bar{2}0)$, was done in order to understand the influence of CVD α-alumina coating textures on the ability of the coatings to deform plastically at different locations on the rake face of a cutting tool insert during a metal machining operation.

Schmid factor diagrams were constructed using MATLAB/MTEX in order to visualize the angular dependence of an external force relative to the α-Al_2O_3 crystals (grains) on the Schmid factor. The diagrams were also used to extract m-value frequency distributions for different slip systems and textures. In addition, lateral m-value distribution maps were obtained from experimental textured coatings using electron backscatter diffraction. These maps show the ability for neighboring grains to deform plastically in the coatings.

Cutting tool inserts with differently textured α-Al_2O_3 coatings were subjected to dry machining of a quench-tempered steel. Using scanning electron microscopy, the microstructure and surface topography of the worn alumina layers were investigated and it was found that a flatter surface morphology and higher probability of discrete plastic deformation are connected to less wear. This was observed in the (0001)-textured sample, which also exhibited the highest m-values in the wear zone with highest temperatures and external forces. It was observed that basal slip is most easily activated, followed by prismatic slip systems 1 and 2 in this case. For $(01\bar{1}2)$ and $(11\bar{2}0)$ textured coatings the differences in m-values for the three slip systems are not that big, and the distributions are relatively wide.

It is clear that the Schmid factor analysis forms a basis that is important for understanding crater wear, especially when it is connected to local plastic deformation, of textured CVD α-Al_2O_3 coatings. The methodology of this work can be expanded to other coating systems and also more generally to applications where it is of interest to analyze the deformation behavior and local plastic anisotropy of textured materials.

1. Introduction

Tools for metal cutting must withstand severe operating conditions as they are subjected to high loads, high temperatures, large temperature gradients, thermal shock, fatigue, abrasion, attrition and diffusion wear. It has previously been found that wear-resistant coatings significantly improve cutting tool properties and life [1,2]. These coatings are often produced by CVD (Chemical Vapor Deposition). Typical coating materials are TiC, Ti(C,N), TiN, alumina and TiAlN. CVD alumina coatings deposited on cemented carbide cutting inserts are widely used for turning of steel due to their excellent properties, such as chemical inertness, mechanical and thermal stability, low thermal conductivity and high hardness at elevated temperatures, ~650 °C to 1100 °C, which is the typical range in metal cutting applications [3–8].

Early CVD alumina coatings were usually a mixture of several polymorphs with metastable κ-Al_2O_3 being the most commonly occurring phase [9–11]. Later, both pure κ-Al_2O_3 and α-Al_2O_3 coatings could be deposited in a controlled way by CVD [12–14]. The properties of CVD α-Al_2O_3 coatings have been significantly improved through optimizing the underlying so-called bonding layers for phase control, as well as performing microstructural refinements in the coating layers, *e.g. via* lowering the fraction of pores at interfaces, see for example references

* Corresponding author at: Department of Physics, Chalmers University of Technology, Gothenburg, Sweden.
E-mail address: siamak.shoja@sandvik.com (S. Shoja).

https://doi.org/10.1016/j.surfcoat.2021.126991
Received 9 October 2020; Received in revised form 11 February 2021; Accepted 12 February 2021
Available online 27 February 2021

[4,5,15–20]. Further development led to highly textured α-Al_2O_3 coatings [5], which improved their properties, resulting in even better performance and tool life. The wear properties of CVD α-Al_2O_3 layers with different growth textures were studied by Ruppi [21] and M'Saoubi et al. [22]. They suggested that the ability for the coating to undergo plastic deformation was limiting the amount of degradation (wear), due to for instance less cracking and flaking. Ruppi et al. [21,23] examined the ability to undergo uniform plastic deformation for α-Al_2O_3 coatings with a number of textures, namely $(10\bar{1}2)$, $(10\bar{1}4)$, (0001) and $(10\bar{1}0)$. They reported that the (0001)-textured coatings exhibit better wear performance as compared to the other textured coatings. Thus, in order to understand the limiting factors in many machining applications, *i.e.* crater wear, we need to understand the underlying mechanisms for the ability for textured CVD α-Al_2O_3 coatings to undergo plastic deformation, which is the aim of this paper. A short turning test was designed to only wear the α-alumina coating and thus, substantial plastic deformation of hardmetal, which has a major role in ending the machining tool life [24], was not in the scope of this work.

The plastic deformation of corundum (α-alumina) has been studied extensively [25,26]. Analysis of dislocation configurations in samples deformed mostly at high temperatures shows that dislocation glide is the main mechanism at low and moderate temperature. Other studies have concerned mainly creep deformation, diffusion creep and diffusion-controlled grain boundary sliding at temperatures higher than 1200 °C [27–29]. These mechanisms will not be discussed here as our focus is on metal cutting applications, where temperatures are in the lower temperature range, *i.e.* around 600–1100 °C, depending on cutting conditions and exact location on the cutting tool insert. In steel turning, the temperature on the flank face of the cutting tool insert is generally 200–300 °C lower than on the rake face [30]. Therefore, the crater wear that occurs on the rake face is more connected to plastic deformation of the coating, while flank wear is more related to abrasion. There are three different wear zones on the rake face; sticking, transition and sliding zones, with the highest temperatures at the end of the transition zone. The probability for plastic deformation in the different zones, with different loading conditions and temperature, will be treated in this paper.

There are three slip systems that are commonly active at high temperatures: $\{0001\}\frac{1}{3}<11\bar{2}0>$ basal slip [26,31,32], $\{11\bar{2}0\}<\bar{1}100>$ and $\{11\bar{2}0\}\frac{1}{3}<\bar{1}101>$ prismatic slip [31–37] and $\{10\bar{1}1\}<\bar{1}101>$ pyramidal slip [32,33,38]. Basal and prismatic slip have been activated in special cases, such as under hydrostatic confining pressure, also at low temperatures, 600 °C and 200 °C, respectively [25,36]. The number of active slip systems is limited in the temperature range associated with metal cutting, and α-Al_2O_3 might therefore exhibit brittle or ductile behavior, depending on the exact loads, geometry and temperature during the cutting operation.

For the basal and prismatic slip systems, the critical resolved shear stress (CRSS) follows a logarithmic dependence with temperature [39]. However, the slopes of the two lines corresponding to the logarithmic CRSS values *versus* temperature for basal and prismatic slip systems, are different and they intersect at 600–700 °C; above this temperature range basal slip is preferred, with a lower shear stress needed for activation. Data from several studies suggest that prismatic plane dislocations ($\{11\bar{2}0\}<\bar{1}100>$) dissociate in their slip planes into three collinear partials at low temperature (≈400 °C) [25,40,41]. This behavior of low-temperature plastic behavior is not extended to temperatures above 700 °C. At these higher temperatures, basal slip is the easiest slip system to activate.

It is necessary to calculate the resolved shear stress (RSS) in order to understand if slip is possible. RSS depends on the Schmid factor, which depends on the loading conditions (which are different in the different rake face zones), *i.e.* the direction of the external force (coming from the chip formation and glide during machining), coating texture (grain orientations) and the slip system (Burgers vector and glide plane) that the Schmid factor is calculated for.

The aim of this paper is to understand the influence of a CVD α-alumina coating texture on the ability of the coating to deform plastically at different locations on the rake face of a cutting tool insert during a metal cutting operation. This will be done by a thorough analysis of the Schmid factors for three different (basal and two prismatic) slip systems, and three different coating textures (0001), $(01\bar{1}2)$ and $(11\bar{2}0)$. The values obtained for ideal textures will be compared to three experimental CVD coatings with these textures. The results for differently textured coatings will be compared and related to observed deformation behavior.

2. Materials and methods

2.1. Materials

The studied CVD coatings were prepared in an industrial scale hot wall CVD reactor of type Bernex 530 L with overall dimensions of 1600 mm height and 530 mm diameter, with an approximate capacity of 10,000 inserts per batch. The coatings were comprised of several sub-layers obtained from different processing steps, and were deposited on WC-Co substrates using thermally activated CVD. They consisted of an inner TiN layer, ~0.3 μm thick, deposited at 860 °C, followed by a medium temperature CVD Ti(C,N) layer with a thickness of ~6 μm, deposited at 860 °C from $TiCl_4$ and CH_3CN. Next a bonding layer (Ti(C,N,O)) with a thickness of ~0.5 μm was deposited at 1000 °C using $TiCl_4$, N_2, CH_3CN and CO as precursors, followed by an α-Al_2O_3 layer of ~5 μm thickness that was deposited at 1000 °C using $AlCl_3$, CO_2 and H_2 as precursors together with additions of different amounts of H_2S and CO during the nucleation and growth steps to produce the desired textures: (0001), $(01\bar{1}2)$ or $(11\bar{2}0)$ [5,21,42,43].

The microstructure and surface morphology of the samples were investigated using Scanning Electron Microscopy (SEM). Special attention was paid to the surface topography of the worn (see below) alumina layers at different wear zones on the rake face. The texture and Schmid factors of the as-deposited α-Al_2O_3 coatings, close to the cutting corner on the rake face, were analyzed using pole figure analysis and inverse pole figure (IPF) and Schmid factor mapping, based on Electron Backscattered Diffraction (EBSD) data from the unpolished coating surface. Details of the wear tests, specimen preparation and the imaging and analytical techniques are given below, while the results for the different samples are presented and discussed in Section 3.

2.2. Metal cutting experiments and electron microscopy characterization

The three differently textured coatings were tested by machining of a quenched-tempered steel workpiece material in single point dry turning using a modern CNC lathe. All three samples had an ISO tool geometry of CNMG 120408-PM, and were used in longitudinal dry turning for 2 min. A cutting speed (v_c) of 220 m/min, a feed rate (f) of 0.2 mm/rev, and a depth of cut (a_p) of 2 mm were used for all three samples. The workpiece material was 100CrMo7–3 with the main elements of C: 0.96, Si: 0.26, Mn: 0.67, Cr: 1.67, Ni: 0.15, Mo: 0.23, Al: 0.34 in wt%. A Zeiss Ultra Field Emission Gun (FEG) SEM was used to examine both as-deposited and worn inserts.

2.3. X-ray Diffraction (XRD)

X-ray Diffraction (XRD) measurements were done with a Bruker D8 Advance instrument using CuK_α radiation. The XRD was used with a θ-2θ scan setup. Using the XRD measurements, textures for the alumina layers were evaluated using texture coefficients, TCs, which were calculated according to Harris formula, see Eq. (1). The equation uses the intensity ratios of diffraction peaks (hkl) from possibly textured coatings over non-textured coatings, in order to calculate the degree of texture.

$$TC(hkl) = \frac{I(hkl)}{I_0(hkl)} \left\{ \frac{1}{n} \sum \frac{I(hkl)}{I_0(hkl)} \right\}^{-1} \quad (1)$$

I(*hkl*) is the measured integrated area intensity of the *(hkl)* reflection with corresponding reference intensity I_0(*hkl*), and *n* is the number of reflections used in calculation. The (hkl) reflections used are $(10\bar{1}4)$, $(11\bar{2}0)$, $((11\bar{2}3))$, $((02\bar{2}4))$, $(11\bar{2}6)$, $(01\bar{1}8)$, $(03\bar{3}0)$, $(0\,2\,\bar{2}\,10)$, $(0\,0\,0\,12)$ and $(0\,1\,\bar{1}\,14)$ and their corresponding reference intensities according to the α-Al_2O_3 PDF card 10–0173, used are $I_0(10\bar{1}4) = 10{,}000$, $I_0(11\bar{2}0) = 4686$, $I_0(11\bar{2}3) = 9734$, $I_0(02\bar{2}4) = 4903$, $I_0(11\bar{2}6) = 9562$, $I_0(01\bar{1}8) = 724$, $I_0(03\bar{3}0) = 5632$, $I_0(0\,2\,\bar{2}\,10) = 728$, $I_0(0\,0\,0\,12) = 168$ and $I_0(0\,1\,\bar{1}\,14) = 448$, which makes the maximum value of the texture coefficient equal to 10. This value corresponds to a perfectly oriented material. In contrast, the value of 1 corresponds to a randomly oriented sample.

2.4. Electron Backscatter Diffraction (EBSD)

Grain orientation and Schmid factor mapping of the alumina layers were performed by means of EBSD. This enabled us to carry out high resolution microstructural (grain size and shape) and micro-textural (preferred orientation of α-alumina grains) analyses of the samples. The EBSD analyses were performed on the top surfaces of the as-deposited alumina layers. The analyses were performed using an Aztec Oxford EBSD system with a NordlysNano detector, mounted on a Tescan GAIA3 dual beam Focused Ion Beam (FIB)/SEM instrument. In order to have good statistics for texture and Schmid factor analysis, areas of 50 μm × 50 μm with 200 nm step size at 20 kV operating voltage were analyzed. Texture and Schmid factor analyses of the EBSD measurements were performed using the HKL Channel 5 (Oxford Instruments) software. For texture analysis and calculating inverse pole figures half-

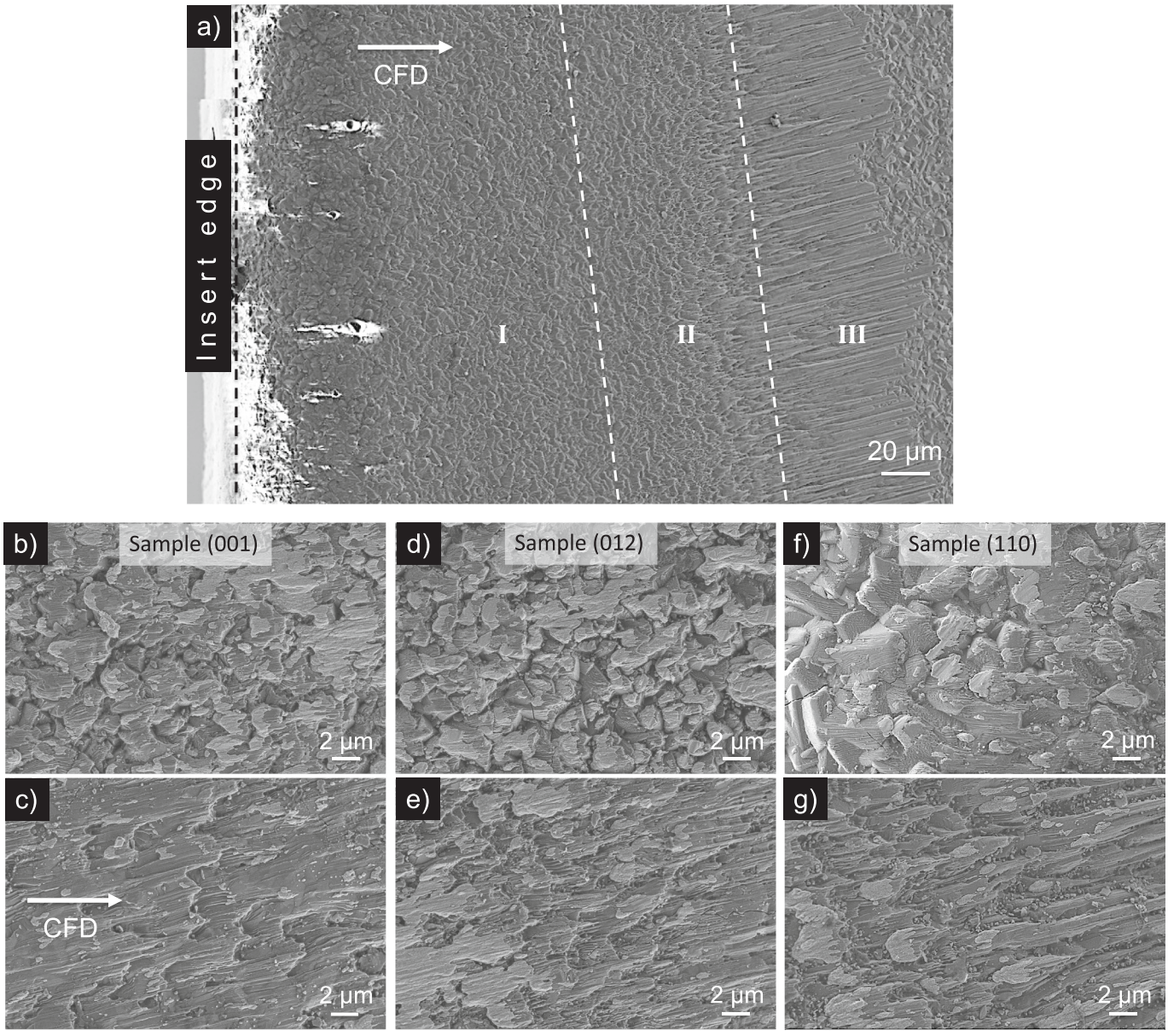

Fig. 1. (a) SEM overview showing the worn rake face surface on Sample (110). The different wear zones I–III corresponding to sticking, transition and sliding zones are marked. The chip flow direction (CFD) and edge of the insert are also marked. (b), (d) and (f) Surface morphology at the beginning of the sticking zone (zone I) for the three 001, 012 and 110 samples in larger magnification respectively. (c), (e) and (g) Surface morphology at the end of the transition zone (zone II) for the three 001, 012 and 110 samples in larger magnification respectively, showing ridge-shaped elongated features. The brighter parts consist of adhered workpiece material. The chip flow direction (CFD) is from left to right in all images.

width of 10° and cluster size of 5° were used. The ratio of unindexed Kikuchi patterns was about 15–25%, which was smoothed in the IPF maps.

Theoretical Schmid factor calculations were performed using MATLAB and MTEX toolbox [44]. The Schmid factor is the ratio between the shear stress on a slip plane in a slip direction and the tensile (or compressive) stress that generates this shear stress. Its value depends on the angles between the tensile stress direction and the slip plane normal, and between the tensile stress direction and the slip direction, and it has a maximum of 0.5 when both these angles are 45°.

3. Results

3.1. Wear results

As mentioned above, both theoretical and experimental analysis of Schmid factors based on three common slip systems and three different textured coatings were made, using the MATLAB MTEX Toolbox for theoretical calculations and the SEM EBSD technique for experimental data. The results for all three textures are presented and discussed in this section.

SEM micrographs of the rake face after 2 min dry turning at 220 m/min are shown in Fig. 1. The surface on the rake face exhibits three different wear zones, appearing along the chip flow direction, each displaying its own pattern and characteristic features. The chip flow direction and different wear zones are marked in Fig. 1a, where the zones I–III correspond to (I) the sticking zone near the edge, followed by (II) the transition zone in the middle of the chip/insert contact length, and (III) the sliding zone at the end of the contact showing apparent sliding/abrasive wear. The worn rake face of the tools for all three samples are shown in higher magnification in Fig. 1b–1g. Fig. 1b, d and f show the surface morphology of the worn coatings at the beginning of the sticking zone (zone I) in the three samples, while Fig. 1c, e and g show the surface morphology of the worn coatings for the sample samples at the end of transition zone (zone II). As shown in Fig. 1c, e and g the ridge-shaped features are starting to elongate in the chip flow direction and are more plastically deformed at the end of the transition zone and beginning of the sliding zone (between zone II and III), as compared to zone I (Fig. 1b, 1d and 1f). It is apparent that Sample (001) is worn more uniformly compared to the other two (Sample (012) and (110)) in zone II, as it exhibits more flat surfaces with uniformly tapered ridges. It is known that loading conditions (both the load magnitude and angle) are different along the rake face, creating the different wear zones with distinctive wear patterns [22,45], see more details below. It has also been reported that the temperature is highest at the end of zone II [46].

The wear of the coatings after 2 min of turning was measured by cross-section SEM investigations (not shown). It was observed that the wear was highest at the end of zone II, as expected, for all three samples. However, the wear of Sample (001) was almost half, as compared to Sample (012) and (110). In Sample (001) around 2 μm of the alumina layer was worn away in zone II, while in the other two around 4 μm was gone. These results show that there is an association in zone II between the ridge-shaped, elongated surface features and higher wear rates, while a flatter surface morphology is connected to less wear (compare Fig. 1). As pointed out earlier [21,22,47–49], which also can be seen in Fig. 1, there is a higher probability for discrete plastic deformation to occur of coating asperities in zone II than in the other zones.

3.2. Basis for the Schmid factor analysis

A number of studies have shown that the temperature and stress distribution on the rake face of cutting tools are non-uniform [46,50,51]. This is due to the fact that the magnitudes and ratios of normal and tangential stresses are different in the three wear zones. It has been reported that the normal stress decreases from the edge of the tool to the end of the contact length, while the tangential stress is highest somewhere in the middle of the contact [45]. This results in inclination angle changes for the resulting force, from the edge of the tool to the end of the contact length, as schematically shown in Fig. 2. The angle of the resulting force is closer to the surface normal near the edge of the tool; in the sticking zone. The inclination angle (with respect to the surface normal) gradually increases towards the transition zone, until it reaches its maximum and then remains almost constant to the end of the sliding zone. M'Saoubi et al. [45] have shown that the inclination angle of the resulting force begins at ~10° in the sticking zone and reaches about 45° at the end of transition zone and in the sliding zone. These angles have a significant effect on the calculation of the Schmid factor and thus these values (10° and 45°) are used in our Schmid factor calculations below. It is worth mentioning that M'Saoubi et al. have used an insert with the total rake angle of 0°. In this study we have used inserts, which have an ISO tool geometry of CNMG 120408-PM. The rake face in this case has an angle of −7°. However, there is a rake angle of +6° when using a tool holder with these inserts and thus, the total angle on the rake face would be −1°, which makes the results in this reference comparable with our work.

As mentioned above, the number of active slip systems responsible for plastic deformation of α-Al_2O_3 is limited in the temperature ranges typical for metal machining applications. Previous studies have shown that basal slip ($\{0001\}\frac{1}{3}<11\bar{2}0>$, where b = 4.75 Å) and two prismatic slip systems ($\{11\bar{2}0\}\frac{1}{3}<\bar{1}101>$, b = 5.12 Å and $\{11\bar{2}0\}<\bar{1}100>$, b = 8.22 Å) are the most probable slip systems for α-Al_2O_3 in these cases [33,35,36]. The Schmid factors (m) for these slip systems can be calculated by the following relation:

$$m = cos\phi cos\lambda$$

where ϕ is the angle between the loading direction and the slip direction, and λ is the angle between the loading direction and the slip plane normal. Fig. 3a shows schematically the relation between loading axes and the specific slip planes for the basal slip and the two prismatic slip systems. The loading direction is shown as a function of ψ, which is the azimuthal angle (around the surface normal) that changes from 0 to 360° and θ, which is the polar angle, which changes from 0° (normal force) to 90° (force along the surface).

As an example, the results of the calculations of the Schmid factor m for the basal slip system and its three Burgers vectors when the polar angle θ changes from 0 to 90° (with $\psi = 0$) are plotted and shown in Fig. 3b, as well as a calculation at a fixed polar angle $\theta = 45°$ when the azimuthal angle ψ changes from 0 to 360°, which is shown in Fig. 3c. Only the absolute value of m is shown, since shear during dislocation slip is allowed in both the forward and backward directions [52]. The graphs show the Schmid factor as a function of loading angle. They were calculated for the three Burgers vectors which are mathematically symmetrical to the family of six Burgers vectors in the basal plane. The graph in Fig. 3b shows that the Schmid factor calculated for Burgers vector (i) is always zero since the angle ϕ, which is the angle between loading direction and the slip direction, is always 90°, independent of the load polar angle θ. The graph shows that the Schmid factors for the other two Burgers vectors are identical, starting with 0 at $\theta = 0$, reaching the maximum at $\theta = 45°$ ($m = 0.43$), and decreasing to zero as θ reaches 90°. The graph in Fig. 3c, for a constant $\theta = 45°$, shows that the Schmid factors for all Burgers vector follow "sinusoidal" functions, shifted with respect to each other, with two maxima where $m = 0.5$.

By calculating the absolute value of m for all possible loading directions (theta from 0 to 90, sigma from 0 to 360°), the Schmid factor as a function of loading direction can be obtained for a given slip plane and a particular Burgers vector. The results can be visualized as a circle diagram for each case. Diagrams were calculated for the three Burgers vectors $[1\bar{2}10]$, $[11\bar{2}0]$ and $[\bar{2}110]$ on the basal plane (0001), as shown in Fig. 3d. The data in the circle diagrams are viewed from the top, along the c-axis ([0001] projection). In this image the dotted lines with an

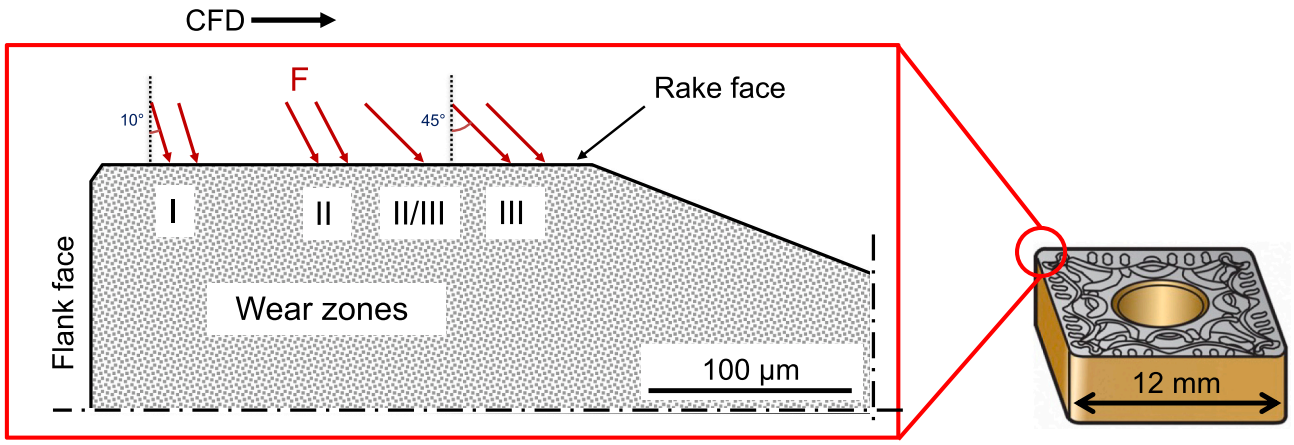

Fig. 2. Schematic drawing of the cutting tool insert showing the different wear zones, the chip flow direction (CFD) and inclination angles of the resulting forces on the rake face.

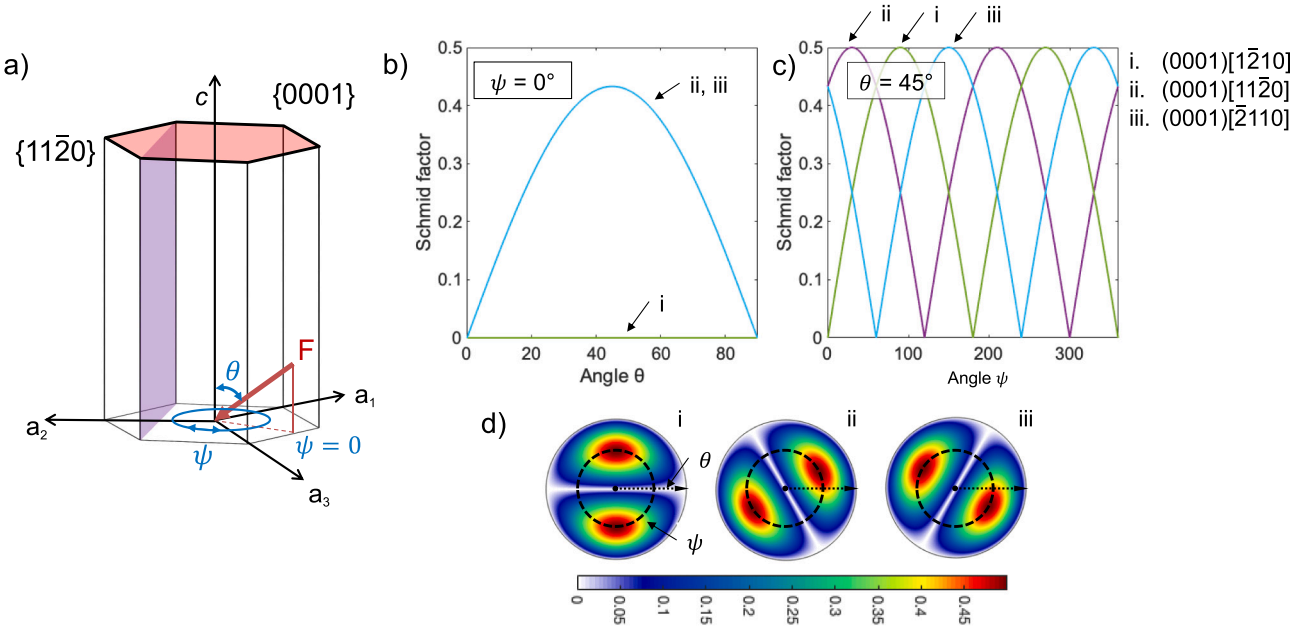

Fig. 3. (a) Schematic drawing of slip systems, loading direction, polar and azimuthal angles (θ and ψ). (b) Schmid factor for basal slip as a function of loading angle θ when $\psi = 0°$. (c) Schmid factor for basal slip as a function of loading angle ψ when $\theta = 45°$. (d) Visualization of Schmid factors for basal slip and the three possible Burgers vectors, dependent of loading direction (θ and ψ). The dotted line with an arrow correspond to angle θ changing from 0 to 90° ($\psi = 0$) and dashed circles correspond to ψ changing from 0 to 360° when $\theta = 45°$. The color legend for the calculated Schmid factor is presented below the circle diagrams.

arrow correspond to an angle θ change from 0 to 90°, with ψ constantly being zero. The dashed circles (counterclockwise) correspond to the angle ψ when it changes from 0 to 360°, while $\theta = 45°$. Thus, the data along these lines and circles correspond to the plots in Fig. 3 b, *e.g.* the data along the dotted lines is for the first case (i) constantly in the white area (Fig. 3d), corresponding to the flat zero-line in Fig. 3b, while for the two other cases (ii, iii) the results are the same, starting at 0, gradually increasing to its maximum value in the red/yellow zone (Fig. 3d), corresponding to m = 0.43 at 45° in Fig. 3b, and then dropping to 0 at the periphery of the circle, where the load is perpendicular to [0001].

By superimposing the diagrams of absolute *m* values calculated for each Burgers vector, a complete diagram of a certain slip system can be obtained, in which the whole family of Burgers vectors are considered. Such diagrams for the three previously mentioned slip systems are calculated and presented in Fig. 4. The resulting diagram for the basal slip system ($\{0001\} < 11\bar{2}0 >$) is shown in Fig. 4a (compare Fig. 3d). The diagram is obtained by combining the absolute *m* values diagrams for $[1\bar{2}10]$, $[11\bar{2}0]$ and $[\bar{2}110]$ Burgers vectors. The maximum absolute value for each point is represented in the final diagram. As mentioned before, only absolute values of three Burgers vectors, out of the total of six, are taken into consideration due to the antipodal symmetry of each pair of Burgers vectors and the fact that both forward and backward slip shear is allowed. The diagram obtained for the whole family of Burgers vectors is representing the slip conditions for one grain when its c-axis is pointing out from the paper ([0001] projection). Similarly to the basal slip diagram, the diagram for prismatic slip system 1 ($\{11\bar{2}0\}< \bar{1}101 >$) is obtained by overlapping the *m* value diagrams for each Burgers vector $[\bar{1}101]$, $[\bar{1}01\bar{1}]$ and $[0\bar{1}11]$ and taking the maximum value of each point, as shown in Fig. 4b. In the same way, the prismatic slip system 2 diagram is shown in Fig. 4c, obtained by combining the diagrams of the $[\bar{1}100]$, $[\bar{1}010]$ and $[0\bar{1}10]$ Burgers vectors.

The diagram in Fig. 4a shows that there are six maxima ($m = 0.5$) positioned at $\theta = 45°$, corresponding to the three pairs of Burgers vectors. There are two regions with $m = 0$; at the center of the diagram,

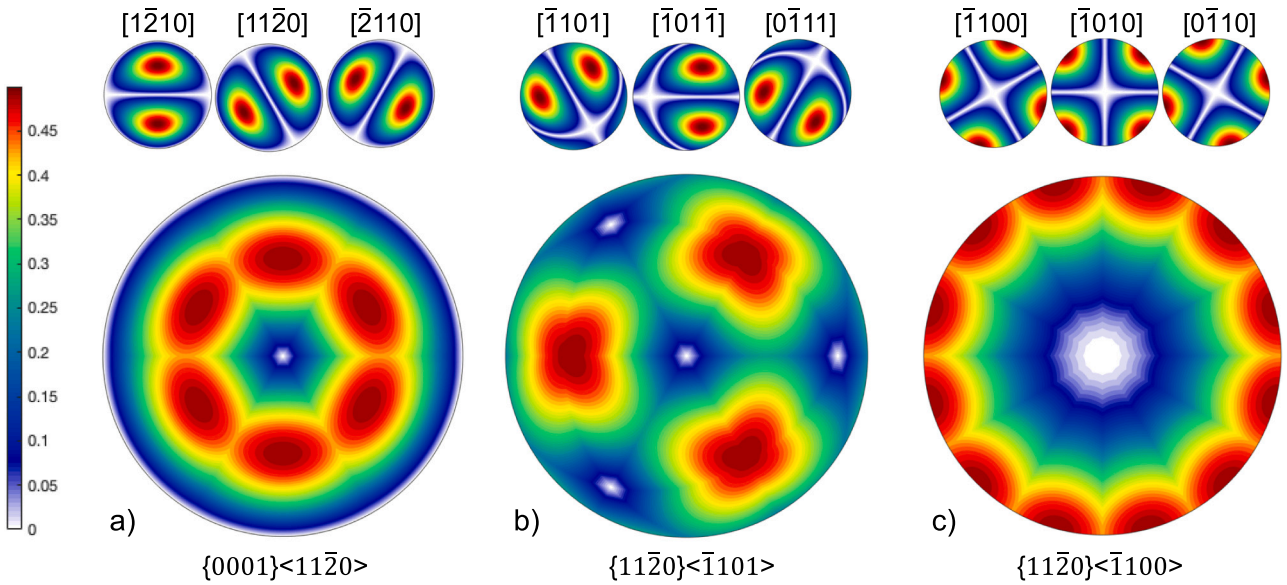

Fig. 4. Schmid factor (absolute values) diagrams (bottom), calculated for (a) $\{0001\} < 11\bar{2}0 >$, basal slip; (b) $\{11\bar{2}0\} < \bar{1}101 >$, prismatic slip system 1 (with short **b);** and (c) $\{11\bar{2}0\} < \bar{1}100 >$, prismatic slip system 2 (with long **b)**. These are constructed by combining the *m* values calculated for the three Burgers vector (top).

corresponding to $\theta = 0$ and at the periphery of the diagram, where $\theta = 90°$, *i.e.* when the load is parallel or perpendicular to the glide plane (0001), respectively. In Fig. 4b however, there are only three red areas, as some of the six maxima partly overlap, rotated 120° with respect to each other at $\theta = 55°$. As a result, the total area with maximum *m* values (red-dark red) is smaller compared to Fig. 4a. There are also small regions with Schmid factors equal to 0; three of them located almost at the periphery of the diagram and one at the center. A rather different shape of the diagram can be seen in Fig. 4c, where twelve half-circled maxima (*i.e.* in total six maxima) are positioned at the periphery ($\theta = 90°$) and a rather larger region with m = 0 is located at the center ($\theta = 0°$), corresponding to a load normal to the glide plane (0001). It is clear from these plots that the ability for plastic deformation, *i.e.* high *m*-values, is very different for the three slip systems for a given load direction with respect to the α-Al_2O_3 crystal orientation. For instance, if the load is perpendicular to [0001], the prismatic slip system 2, as shown in Fig. 4c, has the highest m-values while the for basal slip system the *m* values are zero, as shown in Fig. 4a. This shows that the relative probabilities of plastic deformation can easily be observed in diagrams such as those in Fig. 4. It is important to bear in mind that the actual occurrence of plastic deformation in reality depends not only on the Schmid factors, but also on the temperature, which influences the activation of a given slip system, *i.e.* CRSS, and the magnitude of force, which influences RSS. Together all these factors can reveal if it would be possible to overcome the critical resolved shear stress needed for slip in a particular loading case.

3.3. Schmid factor analysis for ideally textured α-Al_2O_3 coatings

The calculated Schmid factor diagrams can be used to obtain the Schmid factor for one grain with a given orientation of an external force, as described above. For a fiber-textured coating, the use of the diagrams can be extended to visualize the *m* value variation for a fixed external force, depending on grain rotation around the texture direction. The rotation of (an infinite number of) grains relative to a fixed force correspond to a rotation of the force around the coating normal, *i.e.* to azimuthal plots extracted from the circle diagrams at a fixed angle θ, in the same way as described for Fig. 3c. On the other hand, moving from the center of the circle towards its periphery correlates to an inclination of the load from normal (θ = 0°) to tangential (θ = 90°) direction. As stated previously, the loading angle is around 10° in the sticking zone and gradually increases to ~45° at the end of transition and beginning of sliding zones and almost remains around 45° in the sliding zone, which is schematically shown in Fig. 2. Thus, by analyzing all ψ-values we can get the response from all grains in a fiber textured coating, and by choosing an appropriate, constant θ we can investigate the response in a given wear zone.

The diagrams presented in Fig. 4 describe the Schmid factor variation for three different slip systems for an (0001) textured α-Al_2O_3 coating. For that case the (0001) plane normal and the coating normal are at the center of the circle. Similar diagrams can be calculated for other fiber-textures by rotating the coordinate systems, placing the textured grain normals at the center of the circle. Using this technique, we can construct the diagrams by placing (0001), $(01\bar{1}2)$ and $(11\bar{2}0)$ at the center. The resulting Schmid factor diagrams for these three textured coatings, for the basal slip system ($\{0001\} < 11\bar{2}0 >$), the prismatic slip system 1 ($\{11\bar{2}0\} < \bar{1}101 >$) and the prismatic slip system 2 ($\{11\bar{2}0\} < \bar{1}100 >$), are presented in Fig. 5.

The *m* values for the basal slip system for the (0001), $(01\bar{1}2)$ and $(11\bar{2}0)$ textured coatings are shown in Fig. 5a. The two solid circles represent rotating an external force at 10° or 45° inclination around the coating normal, which corresponds to a constant force direction at 10° and 45° in a fiber-textured coating, thus corresponding to the extreme values in Fig. 2. The dashed circles in Fig. 5 correspond to a 10° deviation of grain orientations from the ideal texture, representing a real coating with some small local variations, see more below and compare with Fig. 8. The dashed circles are thus drawn at 10° ± 10° and at 45° ± 10°. By sampling data between the two dashed circles, relative frequency distribution bar plots for the three slip systems in the three textured coatings for the two cases (10° ± 10° and 45° ± 10°) were obtained and they are presented in Fig. 6.

The relative frequency distributions of Schmid factors for the basal slip system for the three textured coatings are shown in Fig. 6a. What is striking about the plots in this figure is at force angle of 45°, the ideally (± 10°) (0001) textured coating shows very high *m* values with a low spread (between 0.4 and 0.5) compared to the ideally $(01\bar{1}2)$ and $(11\bar{2}0)$ textured coatings, which both show very broad spreads of *m* values from 0 to 0.5. This means that at this angle, which is the force angle at the end of the transition zone, activation of basal slip is more probable to occur in (0001) textured coatings compared to the other two ideal textures. A low spread of the *m* values for the (0001) texture also means more

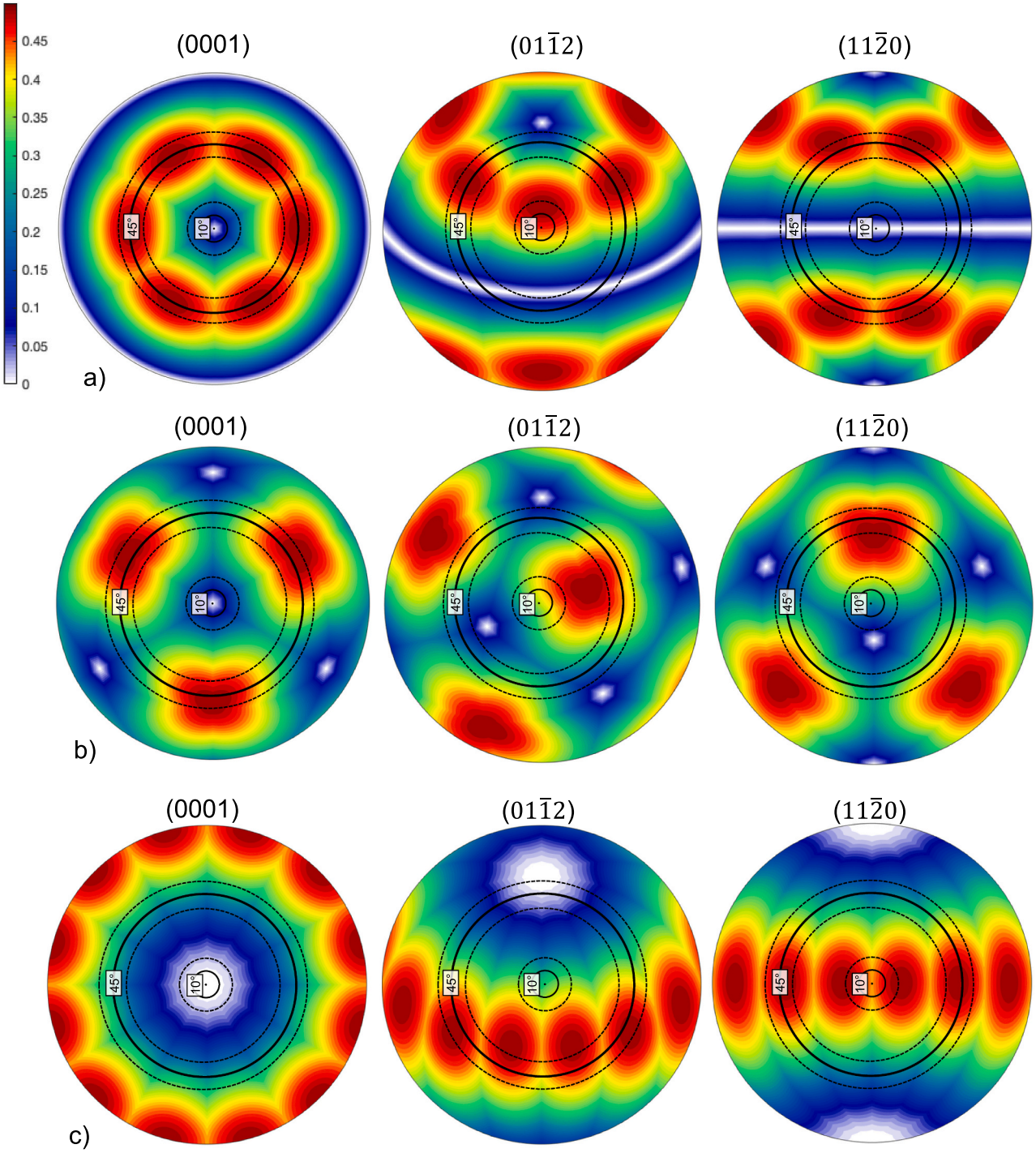

Fig. 5. Resulting Schmid factor diagrams for three textured coatings for (a) $\{0001\} < 11\bar{2}0 >$ (basal slip system) (b) $\{11\bar{2}0\} < \bar{1}101 >$ (prismatic slip system 1) (c) $\{11\bar{2}0\} < \bar{1}100 >$ (prismatic slip system 2). The full circles represent a loading angle of 10° and 45°, corresponding to the sticking zone and transition/sliding zone, respectively. The dashed circles are angles 10° away from the nominal values (10° and 45°). Note that the diagrams for (0001) are 30° rotated compared to Fig. 4.

homogenous slip and deformation in neighboring coating grains, compared to the other two textures that will show quite different slip and deformation response in different grains. Fig. 6a also show that at 10° angle, corresponding to the force angle at the sticking zone, the *m* values are larger for the $(01\bar{1}2)$ texture compared to the other two textures. However, the spread of Schmid factor values is wide (0.2–0.5). In general, it is clear that the ability for basal slip will be very different for all three textures in the different wear zones.

Similar frequency distributions for the prismatic slip system 1 ($\{11\bar{2}0\}< \bar{1}101 >$) are provided in Fig. 6b. From these plots, it can be seen that for this slip system, the relative frequency of *m* values is almost the same at both 10° and 45° with a broad peak at around 0.2–0.4 for almost all cases, especially in the $(01\bar{1}2)$ and $(11\bar{2}0)$ textures. For the (0001) texture, the *m* values are very different at 10° and 45°. This means that activation of prismatic slip system 1 in (0001) texture is quite unlikely to occur in the sticking zone, while it is more likely at the end of the transition zone.

The relative frequency of Schmid factors calculated for prismatic slip

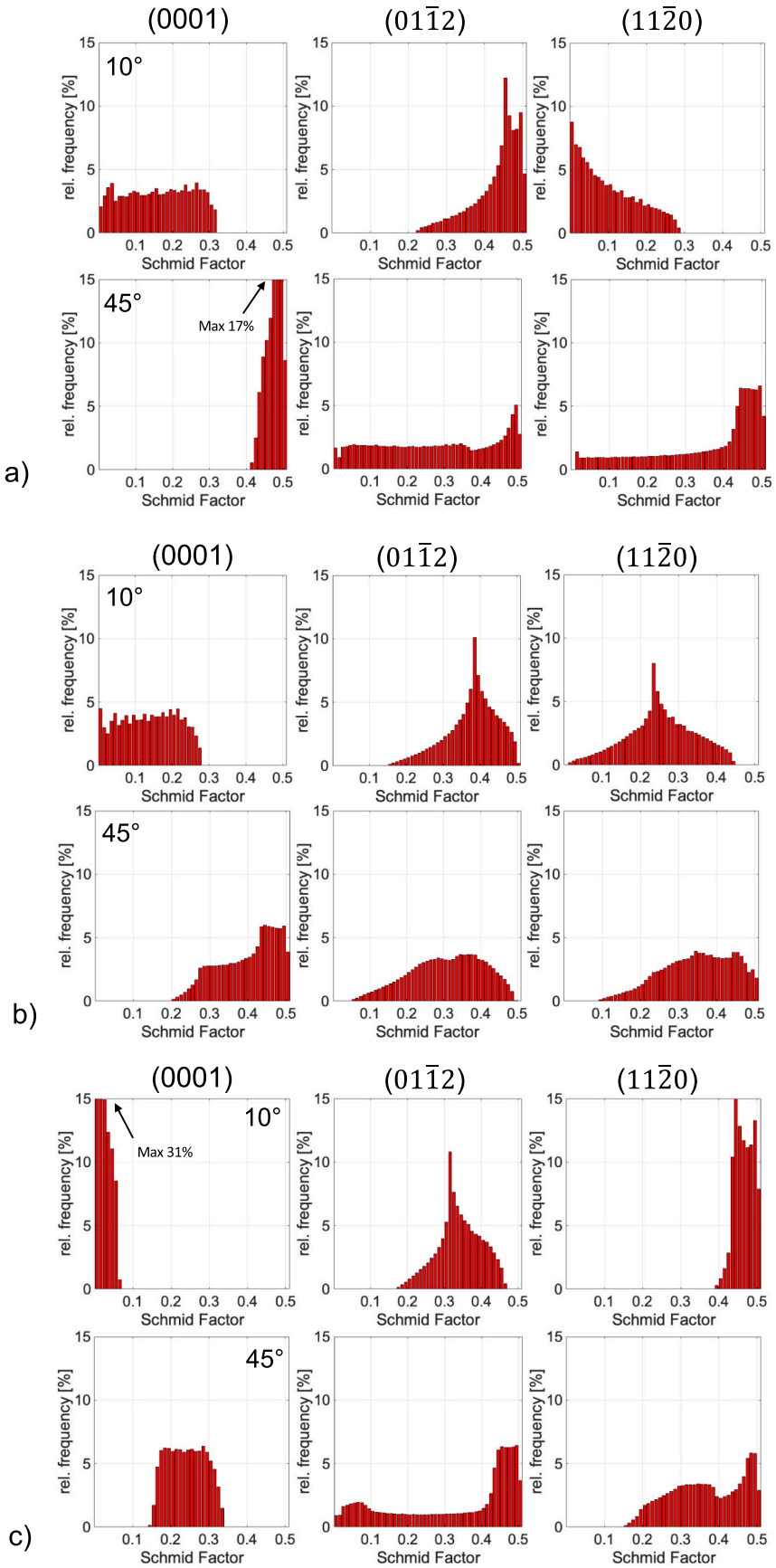

Fig. 6. Frequency diagrams for the calculated Schmid factors for a 10° and 45° inclination angle (± 10°) of the force for three textured coatings considering a) basal slip system, b) prismatic slip system 1 (with short **b)** and c) prismatic slip system 2 (with long **b)**.

system 2 ($\{11\bar{2}0\}<\bar{1}100>$) at 10° and 45° in the three textured coatings are provided in Fig. 6c. It is apparent from these plots that pronounced differences can be observed between the three textures at 10° (sticking zone). For texture (0001) the low values of the Schmid factor suggest that it is very hard to activate $\{11\bar{2}0\}<\bar{1}100>$ in the sticking zone. In contrast, the low spread and high values of Schmid factors in texture $(11\bar{2}0)$ suggest that it is easy to activate prismatic slip system 2 at the sticking zone in this texture. The *m* values in $(01\bar{1}2)$ texture at 10° suggest an average condition for activation of prismatic slip system 2. At 45° however, all three samples show similar behavior for activation of the prismatic slip system 2 with slightly higher probability to activate the prismatic slip system 2 in $(01\bar{1}2)$ and $(11\bar{2}0)$ textures than (0001). A wider spread of *m* values in $(01\bar{1}2)$ texture suggests a more heterogenous slip at 45° loading angle for this texture.

3.4. Texture analysis of the CVD α-Al_2O_3 coatings

The surface morphology of the as-deposited CVD α-alumina coatings with the three ((0001), $(01\bar{1}2)$ and $(11\bar{2}0)$) preferred orientations, *i.e.* Sample (001), Sample (012) and Sample (110), are shown in Fig. 7a–c, respectively, where the original surface morphologies of the coatings are visible. It can be seen from these images that the coatings have similar morphologies. However, Sample (001) has a somewhat smaller grain size, 1–1.5 μm (equivalent circle diameter), compared to the other two samples (1–2 μm for Sample (012) and 2–4 μm for Sample (110)).

EBSD analysis on the rake face of the coated inserts was performed to map the orientation of the grains and to subsequently analyze the Schmid factor distribution of the grains. Inverse pole figure (IPF) maps and inverse pole figures extracted from EBSD data for the three textured coatings are shown in Fig. 8. Almost all grains are red in Sample (001) and very few are observed with yellow or purple colors (the IPF color legend is also shown in Fig. 8). This means that almost all grains are aligned along (0001) and very few grains are tilted away from (0001). This is reflected in the IPF plot for this sample; almost all intensity is located in the (0001) corner. Thus, it is clear from both IPF maps and IPF plots that the grains are highly oriented towards (0001) in this sample.

The IPF map of Sample (012) show more variation in color, see Fig. 8. Numerous grains have some kind of yellow-greenish color, which means that those grains are aligned towards $(01\bar{1}2)$. Many other grains with different colors like green, cyan and light and dark blue can be spotted meaning that these grains are spread between $(10\bar{1}0)$, $(11\bar{2}0)$ and $(01\bar{1}0)$ orientations. These results can be observed in the IPF plot for Sample (012), where most of the intensity is centered around $(01\bar{1}2)$, but some intensity is distributed in the area towards $(11\bar{2}0)$. This means that most grains in the coating have an $(01\bar{1}2)$ orientation, with some deviation towards $(11\bar{2}0)$. In Sample (110) the majority of the grains have cyan, green and blue colors, indicating that almost all grains are centered towards $(11\bar{2}0)$, as also can be observed as an intensity maximum around $(11\bar{2}0)$ in the IPF plot.

Data from Fig. 8 can be compared with the XRD data in Table 1, which shows that the calculated TCs agree well with the IPFs obtained from EBSD for Sample (001) and Sample (110). For Sample (012) the TCs from the XRD data indicates a higher preference for $(11\bar{2}0)$ than for $(01\bar{1}2)$. This could be explained by different sampling volumes for XRD and EBSD. The XRD data comes from the whole coating depth, while the EBSD data comes from outermost part only (< 50 nm). Thus, it is believed that Sample (012) is more $(11\bar{2}0)$ textured in the inner part and more $(01\bar{1}2)$ textured in the outer part. In this work, concerning the Schmid factor analysis, the outer part is most important and Sample (012) can therefore be considered to be mainly $(01\bar{1}2)$ textured in the subsequent analyses.

3.5. Schmid factor analysis of the CVD α-Al_2O_3 coatings

Schmid factor maps of the three textured coating surfaces on the rake face produced from the EBSD data are shown in Figs. 9–11. Schmid factor maps for the basal slip system $\{0001\}<11\bar{2}0>$ at the loading angle of 10° and 45° for the three textured coatings are shown in Fig. 9a and 9b, respectively. The results, as shown in Fig. 9a, indicate that the Schmid factors for the basal slip system is generally slightly higher for Sample (012) than for Sample (001) in the sticking zone. The Schmid factors are lowest for Sample (110), corresponding to a lower probability of basal slip activation for Sample (110). The Schmid factors for basal slip are much higher at the end of transition zone (45°) for all three samples, see Fig. 9b. The values are highest for Sample (001), where almost all grains exhibit high *m* values (low spread in Schmid factor distribution), which can result in a uniform plastic deformation. The *m* values for the Sample (012) and Sample (110) are relatively similar, with values spreading from 0 to 0.5.

Fig. 10a shows Schmid factor maps and frequency distributions when prismatic slip 1 (with shorter Burgers vector, $\{11\bar{2}0\}<\bar{1}101>$) is considered with a loading angle of 10°. It is apparent that the *m* values are highest for Sample (012), while the other two samples are relatively similar. The relatively low *m*-spread in Sample (110) indicates a comparatively uniform deformation response of all grains. The maps at 45° reveal that the *m* values are highest in Sample (001) and (110), as can be seen in Fig. 10b. However, the spread is a little larger in Sample (110). The values are commonly slightly lower for Sample (012).

The Schmid factor maps for the second prismatic slip system (with longer Burgers vector, $\{11\bar{2}0\}<\bar{1}100>$) are presented in Fig. 11. Interestingly, in the sticking zone (Fig. 11a) the *m* values for Sample (110) are very high with a very low spread, while both the values and the spread are really low in Sample (001). Sample (012) also shows high *m* values but with a slightly larger spread. At the transition zone (45°), for this slip system (Fig. 11b), Sample (012) and (110) show high *m* values, but with more spread over the lower values for Sample (012). Sample (001) shows a spread in the *m* values, centered at the mid-range.

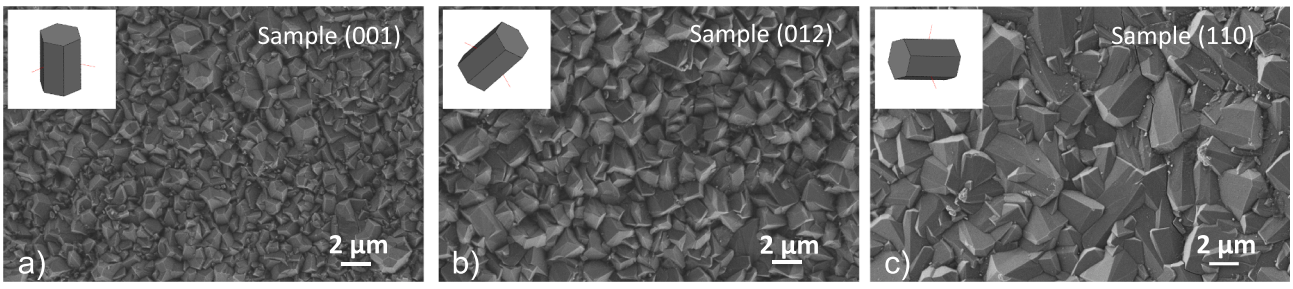

Fig. 7. SEM secondary electron micrographs showing the surface morphology of the three CVD a-alumina coatings. (a) The basal plane (0001) is parallel to the surface. (b) The pyramidal plane $(01\bar{1}2)$ is parallel to the surface. (c) The prismatic plane $(01\bar{1}0)$ is parallel to the surface.

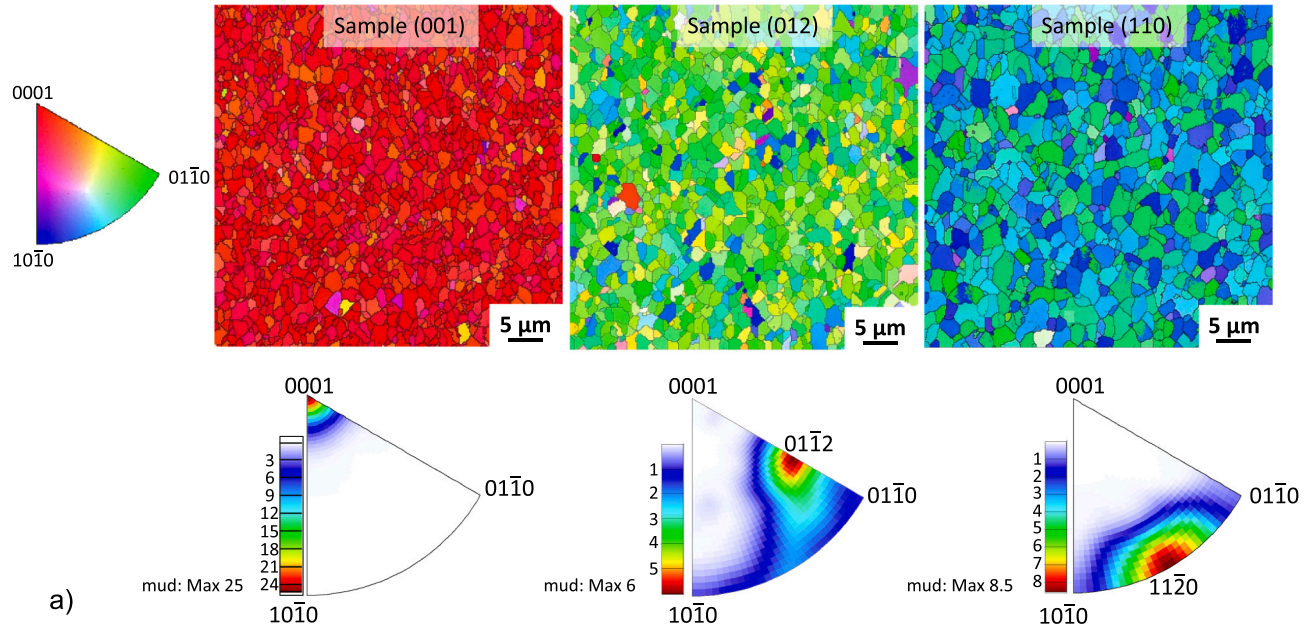

Fig. 8. IPF maps from SEM/EBSD data from the surfaces of the (0001), (01$\bar{1}$2) and (11$\bar{2}$0) textured coatings (top). IPF plots showing the orientation distributions for the three textured coatings (bottom).

Table 1
Calculated texture coefficients for ten reflections showing that all three samples are highly textured. Sample (001), Sample (012) and Sample (110) have high texture coefficients for (0 0 0 12) corresponding to an (0001) texture, mixture of (11$\bar{2}$0) and ((02$\bar{2}$4) corresponding to (11$\bar{2}$0) and (01$\bar{1}$2) textures, and (11$\bar{2}$0) corresponding to a (11$\bar{2}$0) texture, respectively.

TC / Sample ID	$(1\,0\,\bar{1}\,4)$	$(1\,1\,\bar{2}\,0)$	$(1\,1\,\bar{2}\,3)$	$(0\,2\,\bar{2}\,4)$	$(1\,1\,\bar{2}\,6)$	$(0\,1\,\bar{1}\,8)$	$(0\,3\,\bar{3}\,0)$	$(0\,2\,\bar{2}\,10)$	(0 0 0 12)	(0 1 $\bar{1}$ 14)
Sample (001)	0.04	0.21	0.02	0.07	0.03	0.51	0.00	0.08	**6.96**	2.07
Sample (012)	0.05	**4.02**	0.31	**3.27**	0.07	0.35	0.13	0.14	0.27	1.39
Sample (110)	0.03	**7.63**	0.04	0.12	0.02	0.17	0.04	0.05	0.63	1.28

4. Discussion

4.1. General considerations

Previous studies have noted the importance of understanding wear mechanisms and improving the behavior of CVD alumina coatings, *e.g.* by using textured coatings [21–23]. However, very little is found in the literature on the understanding of the underlying deformation mechanisms, especially the effect of the local Schmid factors on plastic deformation of the coatings. In this study we have assessed Schmid factors in different wear zones on the rake face of theoretical, ideally textured CVD α-alumina coated cutting tools, and compared the results with real, textured CVD α-alumina coatings. In addition, we have studied wear of the differently textured CVD coatings after a turning operation for 2 min. Thereby we can get a better understanding of the possibility of local activation of various slip systems and the plastic deformation behavior and wear of CVD α-alumina coated cutting tools.

Alumina is usually considered as a hard, but brittle, material, so it could be expected that it should wear in a brittle fashion, showing cracks and cleavage. However, at temperatures related to metal machining, the surface locally exhibits clear evidence of plastic deformation, see Fig. 1c-g and *e.g.* [21]. Interestingly, the wear rate in the most exposed parts of the surface, *i.e.* the crater wear rate in zone II/III, is less in the coatings with a (0001) texture, where the surface exhibits evidence of more pronounced plastic deformation, see Fig. 1c and [21]. The idea is therefore that by using suitably textured alumina, plastic deformation can be promoted and cleavage avoided, which would give less total wear.

The inclination angle of the applied force changes laterally on the rake face of the inserts (Fig. 2), which affects the Schmid factor locally. Moreover, the coating texture will also influence the value of Schmid factor locally, as it is determined by the angles between the external force and the possible glide planes and Burgers vectors given by the crystal orientation. Thus, both the external load direction and the grain orientation influence the Schmid factor and the associated ability for plastic deformation. For this reason, we have investigated the lateral Schmid factor distribution for three CVD α-alumina coatings with different textures, both theoretically, relating to ideal cases and experimentally for real coatings.

Crater wear occurs on the rake face, where the chip is in contact with the cutting tool. This area is also where the maximum tool temperature is reached. It has been shown that shallow plastic deformation of the coating can take place at the tool/chip contact area [47,53]. These investigations suggest that plastic deformation followed by ductile fracture, possibly combined with dissolution, can be the cause of the crater. However, dissolution usually starts when the α-alumina layer is totally removed, since the solubility of the α-alumina is very low. The ability of plastic deformation depends on the orientation of the textured grains and force angles relative to the coating normal, leading to the different wear zones, as seen in Fig. 1a. Therefore, Schmid factors were calculated for the three most commonly observed slip systems for α-Al_2O_3 for three ideally textured coatings ((0001), (01$\bar{1}$2) and (11$\bar{2}$0)) with 10° and 45° force angles corresponding to the loading situations in the sticking and transition/sliding zones.

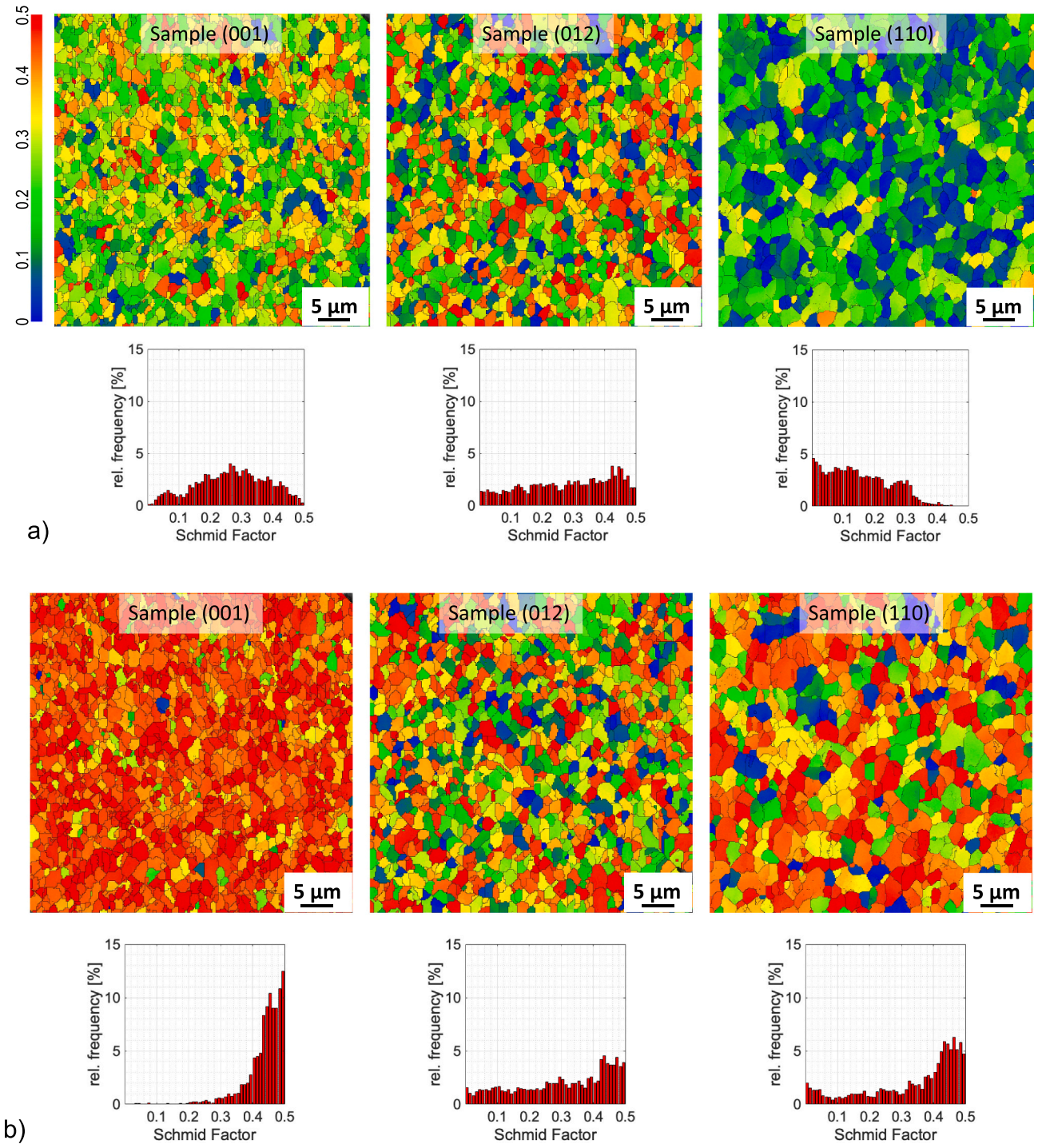

Fig. 9. Schmid factor maps (top) of the rake face surfaces of the textured coatings for the basal slip system $\{0001\} < 11\bar{2}0 >$ with a load angle of (a) 10° and (b) 45° from the surface normal. The Schmid factor frequency distribution (bottom) for each map is also presented.

4.2. Theoretical Schmid factor variations

Schmid factor maps were used as a graphical representation of the calculated Schmid factors for different textures and applied forces. The advantage of these graphs is that they better show the variation of Schmid factors than for instance variations along one direction, compare Fig. 3b and c. The symmetry of the crystal, reflected in the various slip systems, becomes evident in these maps. By combining the results from each Burgers vector in a given slip system, the total response for a grain can be obtained, as for $\{0001\} < 11\bar{2}0 >$ viewed along the c-direction in Fig. 4a. By graphically comparing the results for the basal slip system ($\{0001\} < 11\bar{2}0 >$), the prismatic slip system 1 ($\{11\bar{2}0\} < \bar{1}101 >$) and the prismatic slip system 2 ($\{11\bar{2}0\} < \bar{1}100 >$) in Fig. 4, it is clear that the symmetry of the Schmid factor values is very different for the three slip systems. This means that the influence of the geometry on the ability for the grains to deform plastically will be different. For instance, the prismatic slip system 2 only has high Schmid factors for loads perpendicular to the *c*-axis, corresponding to the red areas along the periphery in Fig. 4c, while the basal slip system exhibits its maxima along a circle at 45° from the c-axis (Fig. 4a). This will in turn lead to different *m*-

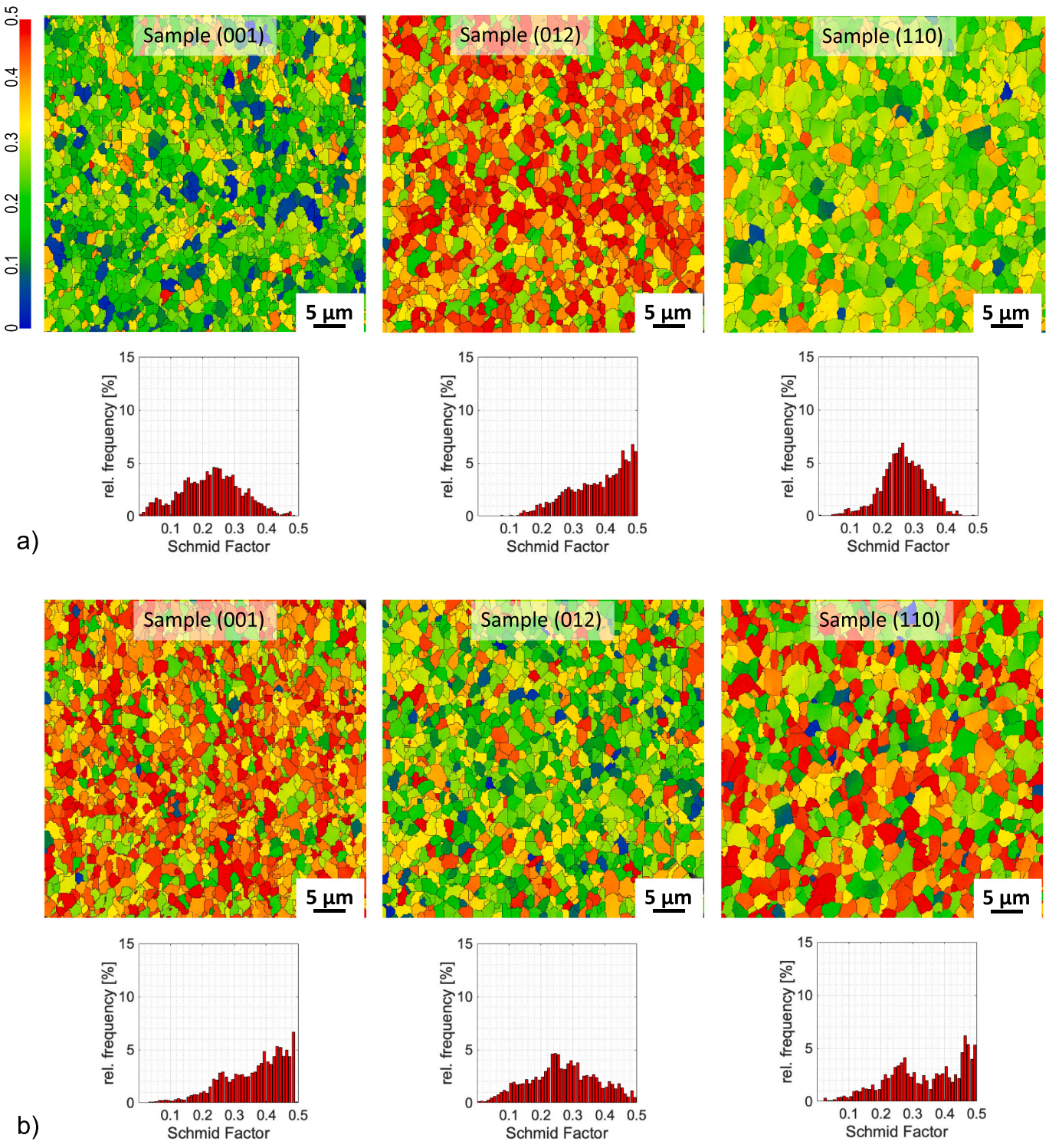

Fig. 10. Schmid factor maps (top) of the rake face surfaces of the textured coatings for the for the prismatic slip system 1 (with short **b)** $\{11\bar{2}0\} < \bar{1}101 >$ with a load angle of (a) 10° and (b) 45° from the surface normal. The Schmid factor frequency distribution (bottom) for each map is also presented.

values for different slip systems, *e.g.* a (0001)-textured coating as Sample (001), compare Figs. 9b and 11b, for a given force direction.

In a similar way theoretical Schmid factor maps can be constructed for the three textures and three slip systems considered in this work, see Fig. 5. In addition to give a graphical representation of the geometrical dependence of the Schmid factors, actual *m*-value data can be retrieved. The maps were used to extract Schmid factor frequency distributions for different slip systems and textures, for ideal cases ±10°, which are the typical angular deviations found in the experimental samples in this work, see Fig. 8. These frequency distributions are very different, depending on texture and loading condition, see Fig. 6. Thus, the ability for the grains to deform plastically will on average be very different in the three wear zones for differently textured coatings.

Knowing that the plastic deformation and crater wear is highest in the transition/sliding zones, where the loading conditions are typically with the force applied 45° from the coating normal, it is worth noting the

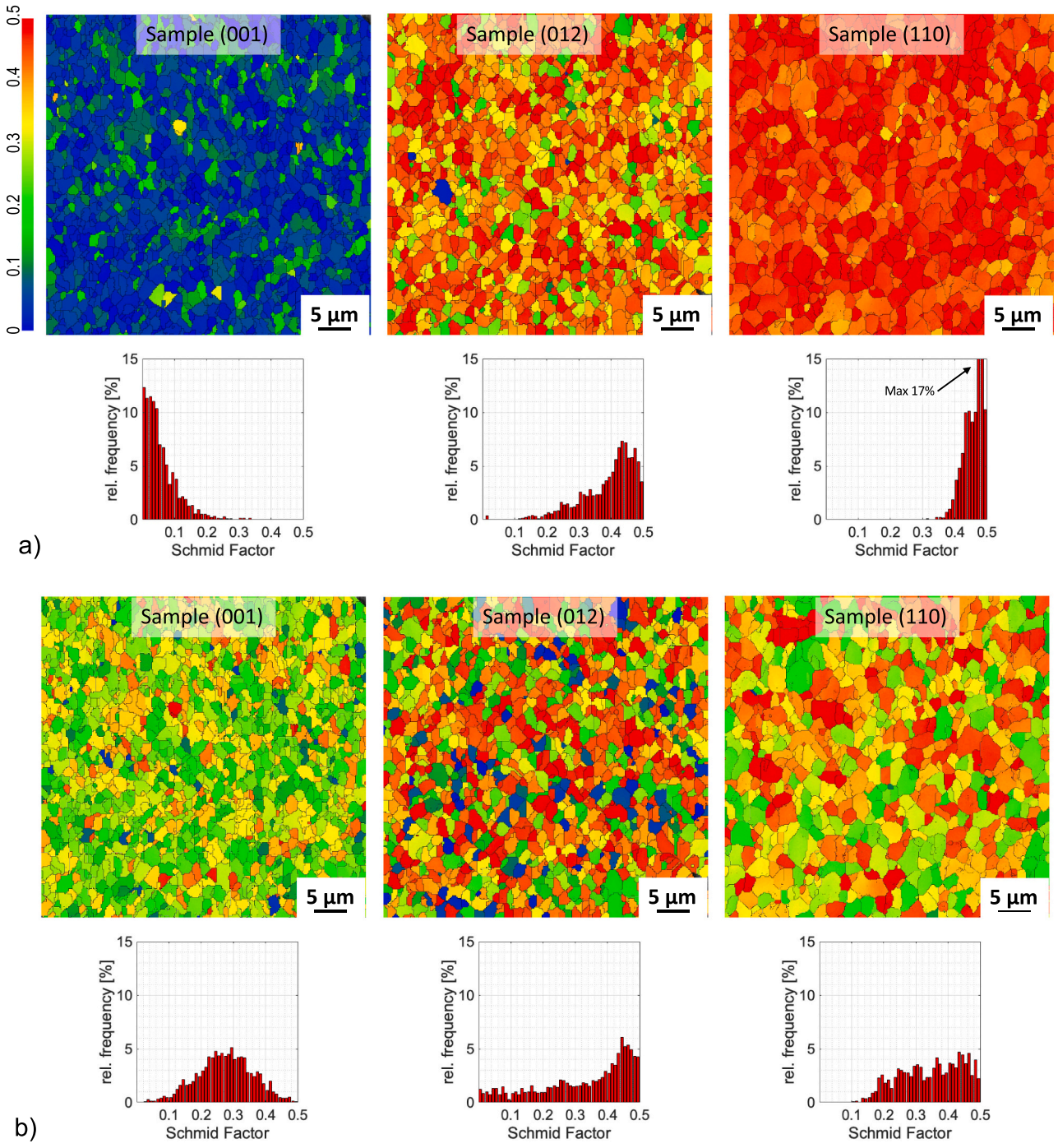

Fig. 11. Schmid factor maps (top) of the rake face surfaces of the textured coatings for the prismatic slip system 2 (with long **b)** $\{11\bar{2}0\} < \bar{1}100 >$ with a load angle of (a) 10° and (b) 45° from the surface normal. The Schmid factor frequency distribution (bottom) for each map is also presented.

different responses for the three ideal textures in this case. From Fig. 6 it is clear that for the (0001)-textured coating the basal slip is most easily activated, followed by prismatic slip systems 1 and 2. For the ideal $(01\bar{1}2)$ and $(11\bar{2}0)$ textures the differences for the three slip systems are not that big, and the distributions are relatively wide.

At a 10° force angle, corresponding to the loading situation at the sticking zone, the results are quite different. For the (0001)-textured coating the Schmid factors are low for all slip systems. For $(01\bar{1}2)$ texture basal slip is most easily activated, followed by prismatic slip 1 and 2. The results are very different for the $(11\bar{2}0)$ texture, as the prismatic slip system 2 exhibits high *m*-values, while prismatic slip 1 shows intermediate values and basal slip exhibits low values, see Fig. 6. Note that these conclusions for Schmid factors are based on the geometry of the loading conditions with respect to the grain orientations. If in a real case plastic deformation will occur or not depends on other parameters as well, such as temperature and load levels. This will be further discussed below.

4.3. Schmid factor analysis for textured CVD α-Al_2O_3 coatings

In order to further visualize the local response of the textured α-Al_2O_3 coatings, experimental coatings were used, see Fig. 8. By performing EBSD and extracting Schmid factor maps for a given load condition, the *m*-values for different grains can be directly visualized, see

Figs. 9–11. Starting at the transition/sliding zones, where the force angle is 45°, we find that for Sample (001), the activation of both the basal slip systems and prismatic 1 slip systems is highly probable compared to other two, Samples (012) and (110), since the *m* values are quite high in Sample (001). The *m* values are also concentrated towards the highest *m*, especially for basal slip, see Fig. 9b, denoting that almost all grains show homogeneous plastic deformation behavior compared to the other two samples, where some grains have very low Schmid factor, indicating that they locally can behave very brittle. These results are consistent with the data obtained in the theoretical calculations of the Schmid factors (compare Fig. 6 with Figs. 9–11), especially for Sample (001) and Sample (110), which had almost all grains with the right orientation, see Fig. 8.

At the sticking zone, due to the smaller angle between the load direction and the surface normal, Sample (001) has lower *m* values compared to its values at the transition zone. The Schmid factors are low and almost similar for the basal and prismatic 1 slip systems. It is, however, almost impossible to activate prismatic 2 slip system in this zone for this sample (Fig. 11a). In contrast, it is very easy to activate prismatic 2 slip in the sticking zone for Sample (110). In this zone, Sample (012) shows slightly lower possibility for activation of basal slip compared to the two prismatic slip systems.

4.4. Notes on plastic deformation

As stated by von Mises (1928), in order to get general plastic deformation, five independent slip systems are required. It should be noted that it is possible to deform a material plastically with only one set of slip systems, *e.g.* basal slip. This would result in the type of deformation happening in the sticking zone, where the morphology of the grains is almost maintained, with only some steps and ridges, as seen in Fig. 1b, d and f. The result of the plastic deformation observed in transition and sliding zone, as seen in Fig. 1c, e and g, where grains are heavily deformed and the surface has a more complex morphology, is only possible by activation of several slip systems. In principle basal slip (3 slip systems, two independent) and prismatic 1 and 2 slip (3 slip systems each, in total only two independent) are not sufficient to get a fully general plastic deformation as this would require also pyramidal slip [54]. However, as seen in the transition/sliding zones, four independent slip systems are certainly sufficient to produce quite substantial plastic deformation.

The more homogeneous and flat-like surface morphology in the transition zone of Sample (001) compared to the other two samples, which have more ridges and valleys, as seen in Fig. 1c, e and g, should be related to the concentration of *m* values towards 0.5 in Sample (001). Sample (012) and Sample (110) show very similar *m* value distributions (but lower than for Sample (001)) in the transition zone for all three slip systems, which also agrees with the similar surface morphology and features observed on the worn coatings of Sample (012) and (110) at the end of the transition zone.

The slip systems are activated at different temperatures [25,36,39]. The three slip systems in our study are probably active, at least to some degree, with the machining parameters given in metal cutting section, since the high local temperatures and extreme machining forces applied on the surface should make it possible to overcome the CRSS required for slip [45,46]. A note of caution is due here, since the applied shear stress is not measured in this work, although it is expected to be sufficiently high, see *e.g.* reference [45]. The different amounts of plastic deformation in the sticking and transition zones can partly be explained by the temperature variations on the rake face during the cutting operation, where the area at the end of transition zone reaches higher temperatures than the sticking zone does. The high plastic deformation at the end of the transition zone is likely to be related to the higher temperature, the associated higher forces and the higher force angle, resulting in easier activation of the slip systems (higher Schmid factors), especially for the basal slip system, as can be seen in Fig. 9b. Since different slip systems are differently active, with basal slip being most activated, different amounts of plastic deformation can be observed in various zones and textures. It can be added that this highly deformed crater wear area can spread towards the edge of the insert and towards the sliding zone if both temperatures and forces increase on the rake face by applying tougher machining conditions than the present case.

A significant observation emerging from the Schmid factor analysis of different textures and slip systems at the transition zone ($45° \pm 10°$) is that the (0001) texture shows very high *m* values and a low spread of for the basal slip system compared to the other slip systems and textures. For this texture, higher *m* values can even be observed for both prismatic slip systems at the transition zone compared to the sticking zone. The observed high *m* values could be connected to the special worn surface morphology at the transition zone of Sample (001) compared to the other two samples. These observations support the hypothesis that high Schmid factors and a low spread of *m* values result in homogenous plastic deformation along the basal planes, creating the flat surface in the transition zone, as can be seen in Fig. 1c compared to Fig. 1e and g. This high degree of plasticity would then be connected to the low wear rate of the Sample (001), about half compared to the other two samples.

The methodology used in this work can be applied and expanded to studies when the stresses in the sample are known. Using the Schmid factors and stress levels the RSS can be calculated and be compared to the $CRSS/_m$ ratio for different slip systems in different wear zones. In addition, by measuring the temperature during the machining process the analysis and prediction of the occurrence of a slip can be done in a more accurate way. The approach of this study can also be expanded to other systems, *e.g.* other textures and/or machining data, and even to other applications where it is of interest to analyze the deformation behavior and local plastic anisotropy of textured materials.

5. Conclusions

In this study we investigated the influence of texture of CVD α-alumina coatings on the ability to deform plastically at different locations on the rake face of a cutting tool insert during a metal cutting operation. Three alumina textures were studied: (0001), $(01\bar{1}2)$ and $(11\bar{2}0)$, and the following conclusions were made using the presented results:

- The Schmid factor analysis forms a basis for understanding crater wear of textured CVD α-Al_2O_3 coatings.
- The ability for plastic deformations in different wear zones, depends on force angles (10° and 45° for sticking and transition/sliding zone) coupled to the orientation of the textured grains.
- Schmid factors (*m*) were calculated for the three most commonly observed slip systems for α-Al_2O_3; the basal slip and two prismatic slip systems.
- Schmid factor diagrams were used as a graphical representation of calculated Schmid factors for differently oriented grains and external forces showing contrasting influence of the geometry on the ability for the grains to deform plastically.
- Schmid factor diagrams were constructed for the three textures and three slip systems. These diagrams were used to extract frequency distributions for different slip systems and textures, both in ideal cases (theoretically) and for CVD grown coatings.
- The extracted frequency distributions are very different, depending on texture and loading condition, exposing that the ability for the grains to deform plastically will on average, and locally, be very different in the three wear zones for differently textured coatings.
- At the transition zone, for the ideal (0001)-textured coating as well as in Sample (001), the basal slip is most easily activated, followed by prismatic slip systems 1 and 2. For the ideal and experimental $(01\bar{1}2)$ and $(11\bar{2}0)$-textured coatings the differences for the three slip

systems are not that big, and the Schmid factor distributions are relatively wide.

- At the sticking zone, for the ideal and experimental (0001)-textured coatings, the Schmid factors are low for all slip systems, while for $(01\bar{1}2)$ texture basal slip is most easily activated, followed by prismatic slip 1 and 2. The $(11\bar{2}0)$ texture shows different results, as the prismatic slip system 2 exhibits high *m*-values, while prismatic slip 1 shows intermediate values and basal slip low values.
- The Schmid factor variation in experimental textured coatings are in agreement with those obtained from ideal cases. In addition, the experimental coatings provided maps of the local lateral behavior, *i. e.* the *m*-values from neighboring fiber-textured grains.
- The low wear rate and more homogeneous deformation in Sample (001) compared to the other coating textures can be as a result of maximum plasticity offered by a higher possibility of activation of basal slip and prismatic 1 slip and low spread of Schmid factor values at the transition zone.
- The methodology used in this work can be applied and expanded to studies when the stresses in the sample are known. Thus, RSS can be calculated and the activation of different slip systems in different wear zones can be determined. It can also be expanded to other systems and applications where it is of interest to analyze the deformation behaviors and local plastic anisotropy of textured materials.

Declaration of competing interest

The authors declare that they have no known competing financial interests or personal relationships that could have appeared to influence the work reported in this paper.

Acknowledgements

The authors would like to thank Swedish Foundation for Strategic Research (SSF) for their financial support *via* the contract ID16-0048. This work was performed in part at the Chalmers Materials Analysis Laboratory, CMAL.

References

[1] A.G. King, and W.M. Wheildon, Ceramics in machining processes. Academic Press, 111 Fifth Ave, New York, N. Y. 1966, 327 P, 1966.
[2] O. Knotek, F. Löffler, G. Krämer, Cutting performance of multicomponent and multilayer coatings on cemented carbides and cermets for interrupted cut machining, Int. J. Refract. Met. Hard Mater. 14 (1–3) (1996) 195–202.
[3] S. Ruppi, M. Halvarsson, TEM investigation of wear mechanisms during metal machining, Thin Solid Films 353 (1) (1999) 182–188.
[4] S. Ruppi, Advances in chemically vapour deposited wear resistant coatings. J. Phys. IV France, 2001. **11**(PR3): p. Pr3–847-Pr3–859.
[5] S. Ruppi, Deposition, microstructure and properties of texture-controlled CVD α-Al_2O_3 coatings, Int. J. Refract. Met. Hard Mater. 23 (4–6) (2005) 306–316.
[6] A. Osada, E. Nakamura, H. Homma, T. Hayahi, T. Oshika, Wear mechanism of thermally transformed CVD Al_2O_3 layer, Int. J. Refract. Met. Hard Mater. 24 (5) (2006) 387–391.
[7] J. Garcia, R. Pitonak, The role of cemented carbide functionally graded outer-layers on the wear performance of coated cutting tools, Int. J. Refract. Met. Hard Mater. 36 (2013) 52–59.
[8] C. Mitterer, 2.16 - PVD and CVD hard coatings, in: V.K. Sarin (Ed.), Comprehensive Hard Materials, Oxford, Elsevier, 2014, pp. 449–467.
[9] B. Lux, C. Colombier, H. Altena, K. Stjernberg, Preparation of alumina coatings by chemical vapour deposition, Thin Solid Films 138 (1) (1986) 49–64.
[10] C. Chaifield, J.N. Lindström, and M.E. Sjöstrand, *Microstructure of CVD* - Al_2O_3. J. Phys. Colloques, 1989. **50**(C5): p. C5–377-C5–387.
[11] S. Vuorinen, J. Skogsmo, Characterization of α-Al_2O_3, κ-Al_2O_3, and α-κ multioxide coatings on cemented carbides, Thin Solid Films 193-194 (1990) 536–546.
[12] S.A. Ruppi, Multi-oxide coated carbide body and method of producing the same. 1992, U.S. Patent 5,137,774.
[13] M. Halvarsson, and S. Vuorinen, Epitaxy in Multilayer Coatings of κ-Al_2O_3. Surf. Coat. Technol., 1996. **80**(1): p. 80–88.
[14] A. Larsson, M. Halvarsson, S. Vuorinen, Microstructural investigation of as-deposited and heat-treated CVD Al_2O_3, Surf. Coat. Technol. 94-95 (1997) 76–81.
[15] S. Vuorinen, L. Karlsson, Phase transformation in chemically vapour-deposited κ-alumina, Thin Solid Films 214 (2) (1992) 132–143.
[16] M. Halvarsson, S. Vuorinen, The influence of the nucleation surface on the growth of CVD α-Al_2O_3 and κ-Al_2O_3, Surf. Coat. Technol. 76-77 (1995) 287–296.
[17] S. Söderberg, M. Sjöstrand, B. Ljungberg, Advances in coating technology for metal cutting tools, Metal Powder Report 56 (4) (2001) 24–30.
[18] S. Canovic, B. Ljungberg, C. Björmander, M. Halvarsson, CVD TiC/alumina and TiN/alumina multilayer coatings grown on sapphire single crystals, Int. J. Refract. Met. Hard Mater. 28 (2) (2010) 163–173.
[19] S. Canovic, B. Ljungberg, M. Halvarsson, CVD TiC/alumina multilayer coatings grown on sapphire single crystals, Micron 42 (8) (2011) 808–818.
[20] P.W. Trimby, Orientation mapping of nanostructured materials using transmission Kikuchi diffraction in the scanning electron microscope, Ultramicroscopy 120 (2012) 16–24.
[21] S. Ruppi, Enhanced performance of α-Al_2O_3 coatings by control of crystal orientation, Surf. Coat. Technol. 202 (17) (2008) 4257–4269.
[22] R. M'Saoubi, S. Ruppi, Wear and thermal behaviour of CVD α-Al_2O_3 and MTCVD Ti(C,N) coatings during machining, CIRP Ann. 58 (1) (2009) 57–60.
[23] S. Ruppi, A. Larsson, A. Flink, Nanoindentation hardness, texture and microstructure of α-Al_2O_3 and κ-Al_2O_3 coatings, Thin Solid Films 516 (18) (2008) 5959–5966.
[24] M. Gassner, N. Schalk, M. Tkadletz, M. Pohler, C. Czettl, C. Mitterer, Influence of cutting speed and workpiece material on the wear mechanisms of CVD TiCN/α-Al_2O_3 coated cutting inserts during turning, Wear 398-399 (2018) 90–98.
[25] K.P.D. Lagerlöf, A.H. Heuer, J. Castaing, J.P. Riviere, T.E. Mitchell, Slip and twinning in sapphire (α-Al_2O_3), J. Am. Ceram. Soc. 77 (2) (1994) 385–397.
[26] A.H. Heuer, K.P.D. Lagerlöf, J. Castaing, Slip and twinning dislocations in sapphire (α-Al_2O_3), Philosophical Magazine A 78 (3) (1998) 747–763.
[27] R.M. Cannon, W.H. Rhodes, A.H. Heuer, Plastic deformation of fine-grained alumina (Al_2O_3): I, Interface-controlled diffusional creep, J. Am. Ceram. Soc. 63 (1–2) (1980) 46–53.
[28] A.H. Heuer, N.J. Tighe, R.M. Cannon, Plastic deformation of fine-grained alumina (Al_2O_3): II, basal slip and nonaccommodated grain-boundary sliding, J. Am. Ceram. Soc. 63 (1–2) (1980) 53–58.
[29] P. Gruffel, C. Carry, Effect of grain size on yttrium grain boundary segregation in fine-grained alumina, J. Eur. Ceram. Soc. 11 (3) (1993) 189–199.
[30] D.T. Quinto, Mechanical property and structure relationships in hard coatings for cutting tools, J. Vac. Sci. Technol. A 6 (3) (1988) 2149–2157.
[31] M.L. Kronberg, Plastic deformation of single crystals of sapphire: basal slip and twinning, Acta Metall. 5 (9) (1957) 507–524.
[32] A. Heuer, J. Castaing, Dislocations in α-Al_2O_3, Adv. Ceram. 10 (1984) 238.
[33] J.D. Snow, A.H. Heuer, Slip systems in Al_2O_3, J. Am. Ceram. Soc. 56 (3) (1973) 153–157.
[34] J. Bilde-Sørensen, A.R. Thölen, D.J. Gooc, G.W. Groves, Structure of the <0110> dislocation in sapphire, Philos. Mag. 33 (6) (1976) 877–889.
[35] D.M. Kotchick, R.E. Tressler, Deformation behavior of sapphire via the prismatic slip system, J. Am. Ceram. Soc. 63 (7–8) (1980) 429–434.
[36] J. Castaing, J. Cadoz, S.H. Kirby, Prismatic slip of Al_2O_3 single crystals below 1000°C in compression under hydrostatic pressure, J. Am. Ceram. Soc. 64 (9) (1981) 504–511.
[37] D.J. Gooch, G.W. Groves, Non-basal slip in sapphire, The Philosophical Magazine: A Journal of Theoretical Experimental and Applied Physics 28 (3) (1973) 623–637.
[38] J. Cadoz, B. Pellissier, Influence of three-fold symmetry on pyramidal slip of alumina single crystal, Scr. Metall. 10 (7) (1976) 597–600.
[39] T.E. Mitchell, P. Peralta, J.P. Hirth, Deformation by a kink mechanism in high temperature materials, Acta Mater. 47 (13) (1999) 3687–3694.
[40] J. Cadoz, J.P. Riviere, J. Castaing, T.E.M. observations of dislocations in Al_2O_3 after prism plane slip at low temperature under hydrostatic pressure, in: R. E. Tressler, R.C. Bradt (Eds.), Deformation of Ceramic Materials II, Springer US, Boston, MA, 1984, pp. 213–222.
[41] K.D.P. Lagerlöf, T.E. Mitchell, A.H. Heuer, J.P. Riviere, J. Cadoz, J. Castaing, D. S. Phillips, Stacking fault energy in sapphire (α-Al_2O_3), Acta Metall. 32 (1) (1984) 97–105.
[42] S. Ruppi, Alumina layer with enhanced texture. 2011 Aug 9, U.S. Patent 7,993,742 B2.
[43] S. Ruppi, Texture-hardened alpha-alumina coated tool. 2011 Apr 12, U.S. Patent 7,923,101 B2.
[44] F. Bachmann, R. Hielscher, H. Schaeben, Texture analysis with MTEX – free and open source software toolbox, Solid State Phenom. 160 (2010) 63–68.
[45] R. M'Saoubi, O. Alm, J.M. Andersson, H. Engström, T. Larsson, M.P. Johansson-Joesaar, M. Schwind, Microstructure and wear mechanisms of texture-controlled CVD α-Al_2O_3 coatings, Wear 376-377 (2017) 1766–1778.
[46] T. Obikawa, T. Matsumura, T. Shirakashi, E. Usui, Wear characteristic of alumina coated and alumina ceramic tools, J. Mater. Process. Technol. 63 (1) (1997) 211–216.
[47] P.A. Dearnley, Rake and flank wear mechanisms of coated cemented carbides, Surf. Eng. 1 (1) (1985) 43–58.
[48] G. Brandt, Flank and crater wear mechanisms of alumina-based cutting tools when machining steel, Wear 112 (1) (1986) 39–56.
[49] P.A. Dearnley, V. Thompson, A.N. Grearson, Machining ferrous materials with carbides coated by chemical vapour deposition II: wear mechanisms, Surf. Coat. Technol. 29 (3) (1986) 179–205.
[50] S. Kato, K. Yamaguchi, M. Yamada, Stress distribution at the Interface between tool and chip in machining, Journal of Engineering for Industry 94 (2) (1972) 683–689.
[51] P. Müller-Hummel, M. Lahres, Quantitative measurement of temperatures on diamond-coated tools during machining, Diam. Relat. Mater. 4 (10) (1995) 1216–1221.

[52] S.R. Agnew, Ö. Duygulu, Plastic anisotropy and the role of non-basal slip in magnesium alloy AZ31B, Int. J. Plast. 21 (6) (2005) 1161–1193.
[53] K. Stjernberg, A. Thelin, Wear mechanisms of coated carbide tools in machining of steel, High Productivity Machining: Materials and Processes (1985) 95–104.
[54] G.W. Groves, A. Kelly, Independent slip systems in crystals, The Philosophical Magazine 8 (89) (1963) 877–887.